Design principle and assessing the correlations in Sb-doped Ba0.5Sr0.5FeO3–δ perovskite oxide for enhanced oxygen reduction catalytic performance

Design principle and assessing the correlations in Sb-doped Ba$_{0.5}$Sr$_{0.5}$FeO$_{3−δ}$ perovskite oxide for enhanced oxygen reduction catalytic performance

Naveed Mushtaq[1, 2†], Yuzheng Lu[3], Chen Xia[2], Wenjing Dong[2], Baoyuan Wang[2], Xunying Wang[2],

M.A.K Yousaf Shah[3], Sajid Rauf[2], Nie Jingjing [2], Enyi Hu[1], Haibo Xiao[2*], Rizwan Raza[†5*], Jung-

Sik Kim[6] and Bin Zhu[†1, 2*]

[1]*Jiangsu Provincial Key Laboratory of Solar Energy Science and Technology/Energy Storage joint Research Center, School of Energy and Environment, Southeast University, No.2 Si Pai Lou, Nanjing 210096, China.*
[2]*Faculty of Physics and Electronic Science, Hubei University, Wuhan, Hubei 430062, P.R. China.*
[3]*School of Electronic Engineering, Nanjing Xiaozhuang University, 211171 Nanjing, China*

[4]*Engineering Research Centre of Nano-Geo Materials of Ministry of Education, Department of Materials Science and Chemistry, China University of Geosciences, 388 Lumo Road, Wuhan, 430074, China.*

[5]*Department of Physics, COMSATS Institute of Information Technology, Lahore 54000, Pakistan.*
[6]*School of Aeronautical & Automotive Engineering, Loughborough University, Loughborough LE113TU, United Kingdom*

[1]*Corresponding author, Bin Zhu;*
Email address: zhu-bin@seu.edu.cn; b.zhu@lboro.ac.uk

Tel.: +46 879 07 403; Fax: +46 8204161

[2] *Corresponding author Haibo Xiao;*

Email address: xhb7142@hubu.edu.cn

 [3]*Corresponding author, Rizwan Raza*

Email address: razahussaini786@gmail.com

†These authors contributed equally to this work

Abstract

Lack of fundamental understanding of the oxygen reduction reaction (ORR) hampers the development of effective metal oxide catalysts and advance low-temperature solid oxide fuel cells (LT-SOFCs). In this study, we report Ba$_{0.5}$Sr$_{0.5}$Fe$_{1−x}$Sb$_x$O$_{3−δ}$ (BSFSb, x = 0, 0.05, and 0.1) cathodes designed from both theoretical and experimental aspects to study a good relationship between a material property and enhanced ORR activity. The BSFSb cathode exhibits a very low area-

specific resistance (ASR) of 0.20 Ω cm^2 and excellent power output of 738 mW-cm^{-2} using the Sm$_{0.2}$Ce$_{0.8}$O$_2$ (SDC) electrolyte at 550℃. The Sb ions doping significantly enhances electrical conductivity and reduces its ORR activation energy. First-principles calculations screen the potential of designed perovskite by showing very low vacancy formation energy and shift in O-p and Fe3-d band centers near to fermi level by replacing Fe with Sb ions. Correspondingly, wide range coverage of distributed orbitals at the fermi level in BSFSb cathode promotes charge transfer with lower energy barrier. These results demonstrate that this design can impact the development of highly functional ORR electrocatalysts for LT-SOFCs and other electrocatalyst applications.

Keywords: Perovskite Ba$_{0.5}$Sr$_{0.5}$Fe$_{0.9}$Sb$_{0.1}$O$_{3-\delta}$ cathode; low area-specific resistance ASR polarization; oxygen reduction reaction (ORR); electrocatalyst; LT-SOFC

1. Introduction

Understanding the relationship of oxygen reduction catalytic ($2e^- + 1/2O_2 = O^{2-}$) properties with structural properties in metal oxides has been a longstanding challenge. Traditionally, researchers identify this relationship by varying the bulk structure/composition and examine the impact of the catalytic activity [1-3]. Although these efforts have resulted in some new catalysts but the options beyond bulk control yet have not been fully explored; and these efforts have not succeeded in defining criteria for developing high performance ORR catalysts. However, low temperature solid oxide fuel cell (LT-SOFC) is highly victimized in term of sluggish ORR kinetics at low temperatures (LT < 600°C). During the past several decades, numerous strategies have been investigated to increase the performance of SOFC cathode at reduced temperatures. But challenges are remaining [4, 5].

Limited understanding and rate limiting steps of the ORR on the multi component perovskites used in SOFCs has been a fundamental barrier for detailed molecular modeling [6]. Attempts to understanding the rate limiting ORR steps on perovskite surfaces have faced major challenges due to the complexity of the materials and difficulties in performing in situ characterization of well-controlled cell structure [7, 8]. Therefore, the rate limiting steps and structure-property relationships underlying the ORR on perovskites are far to be well understood, Thus the goal of designing high ORR catalysts for SOFCs operating at LTs is appeared to be a critical challenge at the present [9].

To date, perovskite oxides are the most promising alternative materials to precious metal and composite cathodes. The single phase mixed ionic and electronic conducting (MIEC) perovskite oxides, such as $La_xSr_{1-x}Co_yFe_{1-y}O_{3-\delta}$ (LSCF), $Ba_{1-x}Sr_xCo_{1-y}Fe_yO3$ (BSCF), $Pr_{1-x}Ba_xCoO3$ and $BaCo_xFe_{1-x}O_{3-\delta}$, showed high ORR even at temperatures 650-800 °C [1, 5, 6]. In contrast, BSCF appears to have a high activity for ORR with an approximately 200-fold increased surface exchange coefficient (k) compared with LSCF at 1000 K. Unfortunately, it suffers from

stability problems. Generally, in MIECs, oxygen vacancies significantly influence ORR and charge transport properties [10-12]. In particular, a high vacancy concentration in the lattice and near the surface can provide more active sites (enhanced triple phase boundary) for oxygen incorporation to enhance ORR catalytic properties [13-15]. Most of high-performance cathodes are based on cobalt-containing perovskite oxides and related structures. However, from the viewpoint of durability, their poor structural stability and relatively large thermal expansion coefficients (TECs) lead to limitations for practical application in SOFCs, which is found to be associated with the valence state and spin state transitions of the Co ions present in the B site of all of these materials [16]. Therefore, significant interest in developing low-Co containing content or Co-free SOFC cathodes such as, Fe-based perovskite oxides have attracted considerable attention because of their stability in oxidizing environments and their good electrocatalytic activity towards the ORR.

In addition, many of the studies involve acceptor doping for creating oxygen deficiency to improve ORR catalytic activity. But research by Irvine et al. has shown that perovskite oxides containing high-valence transition metals (Nb, Ti, Mo, V and Cr) in the B-site are more stable over a wide range of partial pressure of oxygen (pO_2), whereas low-valence transition metals (Co, Ni, Cu and Zn) in the B-site typically cause phase decomposition under reducing conditions [17]. Thus, to design a Fe-based perovskite cathode material with excellent stability under all of these conditions, one approach is to lightly substitute Fe with a higher valence metal on B-site of a perovskite structure. [18-20]. Moreover, Aguadero et al. reports that Sb doping in $SrCoO_{3-\delta}$ perovskite oxide enhanced the thermal stability and as well as electrocatalytic performance [21]. The increased acidity in metal oxide can enhance resistance to CO_2 and supress the Sr segregation and relative acidity in these metal oxides can be acquired by the Jeong electronegativity, and the

valence state of the cation [22]. The acidity of respective cations following the order of Sb^{5+} > Fe^{4+} > Fe^{3+} > Fe^{2+} > Ba > Sr^{2+}. Therefore, substitution of high valance Sb for Fe can bring better CO_2 resistance and could reduce Sr segregation. In this regard, the electrochemical properties of Sb doped Ba-Sr-Fe oxides are worth studying for LT-SOFCs [23, 24].

On the other hand, advanced computational methods (first-principles calculation) provide a strong and useful tool to predict the crystal structure and property related to the electron configuration of materials over SOFCs cathodes. Density functional theory is widely employed to calculate the corresponding electronic structures for two processes that govern ionic diffusion in these materials: (i) oxygen vacancy formation energy and (ii) vacancy-mediated oxygen migration can also be characterized [25, 26]. Therefore, combined theoretical and experimental studies provide better understandings to accurately predict ground state properties of the materials [4]. Moreover, energy band plays crucial role in materials properties and for designing functionalities of the materials. The energy band structure is considered the basic criteria almost in each field but unfortunately it is ignored for designing the materials in SOFCs or ORR electro catalysts [27].

In this work, we take the advantage of the flexibility of the physical-chemical properties of the perovskite family to prepared a $Ba_{0.5}Sr_{0.5}Fe_{1-x}Sb_xO_{3-\delta}$ (BSFSb, x = 0, 0.05 and 0.1) based perovskite oxide cathode. We carried out experimentally and theoretically efforts to build description on the prepares material for ORR electro catalytic properties. The synthesized BSFSb cathode exhibits appreciable electrochemical performance at low operating temperatures of 450 - 550°C. Moreover, the effect of Sb doping in term of energy band structure, electron states, electrical properties, oxide ion transport and ORR catalytic activities are investigated. The experimental results have also been verified by advanced computational methods and found that Sb-doping change the oxygen vacancy formation energy and O-p band center, which influences

the overall ORR electrocatalytic properties. The current study demonstrates a successful development of Sb–doped $Ba_{0.5}Sr_{0.5}FeO_{3-\delta}$ perovskite cathode material and provides some new understanding of the ORR mechanism for advanced LT-SOFCs.

2. Experimental Methods

2.1 Powders preparations

Sol-gel chemistry was applied to prepare $Ba_{0.5}Sr_{0.5}Fe_{0.8}Sb_{0.2}O_{3-\delta}$, to get a nonfluid 3D network gel by aqueous metal salts. The stoichiometric moles of Ba $(NO_3)_2 \cdot 6H_2O$, Sr $(NO_3)_2 \cdot 6H_2O$ and Fe $(NO_3)_2 \cdot 9H_2O$ and 20% Sb solution in C_2H_5OH was dissolved in 1 molar solution of Ethylenediaminetetraacetic acid to form a stable aqueous solution by a hydrolysis process with continuous stirring and heating (@200 rpm and 80 °C) conditions. The citric acid $(C_6H_8O_7)$ compound was used as a chelating agent and added into solution to avoid forming a large crystal and aggregates for dissociation of particles. In a typical synthesis, metal salts (e.g., nitrates) combined with $C_6H_8O_7$ and metals get separated. Next, an important feature of the sol-gel process was to convert the solvent filled gel into a dry solid oxide through the xerogel method. After this whole process, metal oxides were achieved simply by pyrolysis in air at 900℃ for 8h with a ramp step of 2.5℃/min.

2.2 Device fabrications

The prepared $Ba_{0.5}Sr_{0.5}Fe_{1-x}Sb_xO_{3-\delta}$ (BSFSb, x = 0, 0.05, and 0.1) and $Ni_{0.8}Co_{0.15}Al_{0.05}LiO_{2-\delta}$ (NCAL) purchased from Bamo Sci. & Tech. Joint Stock Ltd., China was used as cathode and anode respectively. In details, slurries of the BSFSb and NCAL powders were prepared through mixing with glycerol (90% volume ratio) and ethanol (10% volume ratio). About 0.20 g slurry of the prepared material was pasted onto inner side of 13 mm diameter's nickel-foam (Ni-foam) and then desiccated at 130 °C for 2h. Fuel cell devices were fabricated by dry pressing methods using NCAL painted Ni foam as anodes [28], $Sm_{0.2}Ce_{0.8}O_{2-\delta}$ (SDC) powder as electrolytes and our prepared $Ba_{0.5}Sr_{0.5}Fe_{1-x}Sb_xO_{3-\delta}$ (x = 0. 0.05 and 0.1) painted Ni foam as cathodes. In First

step NCAL painted Ni-foam put into a steel mold of 13 mm diameter, followed by 0.30 grams of SDC powder (sintered at 800 °C with relative density of 86%) [29] and at the end BSFSb painted Ni-foam simultaneously were pressed at 220 Mpa for the formation of three-layer cells. The thickness of the cell was 1.5 mm with an active area of 0.64 cm^2. To study the electrolytic effect of Ni-foam on electrodes sides, a fuel cell using only Ni-foam as electrodes with SDC electrolyte was prepared to measure fuel cell performance. To investigate the ORR catalytic activities, symmetrical cells with BSFSb-painted Ni-foam cell was pressed at 200-220 Mpa on both sides of an SDC electrolyte. Ag paste was applied on both sides of the cell as a current collector.

2.3 Characterizations

Bruker D8 (advance diffract-meter) with Cu-Kα radiation (λ=1.5418 Å) and Tecnai G2 F30 S-TWIN 300 kV/FEG Transmission Electron Microscopy (TEM) were used for phase and crystal structure analysis, respectively. Refinements of XRD data were performed using Jade 6.5 software. Surface morphology and chemical composition analysis were performed using field emission scanning electron microscopy (FESEM, JEOL JSM7100F Japan) coupled with an Oxford energy-dispersive spectrometer (EDS) detector. X-ray photoelectron spectroscopy (XPS, Physical Electronics Quantum 2000, Al Kα X-ray source) was employed to collect surface and chemical analysis data, and CASA XPS software was used to analyze the XPS results. Photoluminescence spectroscopy (Raman microscope (RENISHAW UK) and He (I) ultraviolet photoelectron spectroscopy (ESCALAB 250XI, Thermo Fisher Scientific UK) were employed to measure the energy gaps and valance band offset, respectively.

Electrochemical measurements were conducted with Gamry Reference 3000, USA workstation and CHI-730D (pine instruments U.S) to study the oxygen reduction reaction (ORR) under open circuit voltage (OCV) conditions. The electrochemical impedance spectra were

measured in frequency range of 0.1 HZ to 1 M Hz with 10 mV of dc signal. EIS data were further fitted with model circuits using ZSIMPWIN software. The dc conductivity was measured using Keithley 2400 source meter by two probe method. The activation energy (Ea) was calculated using Arrhenius plot of dc conductivity by the following formula:

$$\sigma = \frac{A}{T} \exp\left(-\frac{E_a}{kT}\right)$$

Where A is the pre-exponential factor, T is the absolute temperature, Ea is the activation energy and k are Boltzmann constant. The oxygen non-stoichiometry (δ) at room temperature were determined by iodometric titration. Approximately 0.1 g of the prepared powders was dissolved into ca. 15 ml of 4 M HCl, followed by mixing with 15 ml of 10 wt% KI. As soon as the Fe cations were sufficiently reduced, the resulting solution was titrated with standardized 0.1 M $Na_2S_2O_3$ using a starch solution as the indicator under a N_2 atmosphere. While, The variation in oxygen non-stoichiometry (δ) for the powder samples was determined as a function of temperature using thermo-gravimetric analysis (TGA) methods (The simultaneous thermal analyser 449F3 Netzsch) along with differential thermal analysis (DTA) in air from 30-800°C with ramped step of 1°C/min. According to the TGA data, the oxygen non-stoichiometry (δ) samples at various temperatures was calculated using the following equation [16]:

$$\delta = \frac{M_o}{15.99}\left(1 - \frac{m}{m_o}\right) + \delta_o$$

Where m_o is the starting weight and m is the final weight of the sample under various temperatures during the TGA measurements δ_o is the oxygen non-stoichiometry at room temperature, M_o is the molar mass of the samples at room temperature, and 15.999 is the atomic weight of oxygen atoms. δ_o was calculated by iodometric method at room temperature. The electrochemical performance of prepared fuel cells was measured by IT 8500 dc electronic load

using humidified hydrogen (typically 97% H_2 & ~3% H_2O at 25°C) and air as fuel and the oxidant with common flow rates of 150 mL/min and 100 mL/min), respectively.

2.4 First principle calculations

The density functional theory (DFT) method is employed widely to study the ground state properties and perform vital analysis on the intrinsic mechanism, and good agreement with experimental results was noted. Spin polarized DFT+U theory calculations were performed with Cambridge serial total energy package (CASTEP) on Materials Studio 8.0. Ion-electron interactions were treated using projector augmented-wave potentials and a generalized gradient approximation (GGA) in the form of Perdew-Burke-Ernzerhof and adopted to describe electron–electron interactions. Electron wave functions were expanded using plane waves with an energy cut-off of 520 eV. The Kohn–Sham equation was solved self-consistently with a convergence of 10^{-5}. A $3 \times 3 \times 3$ k-point grid Brillouin zone structure having 135 atoms [25, 26].

Pseudo atomic calculations were performed on Ba ($4s^2$, $4p^6$ $5s^2$), Sr ($4s^2$, $4p^6$ $5s^2$) Fe ($3d^6$, $4s^2$), and Sb ($5s^2$, $5p^3$). The stoichiometry of the simulated systems was set to $Ba_{0.5}Sr_{0.5}FeO_3$, $Ba_{0.5}Sr_{0.5}Fe_{0.95}Sb_{0.05}O_3$ and $Ba_{0.5}Sr_{0.5}Fe_{0.9}Sb_{0.1}O_3$, respectively, due to computational limitations, and the Sb in BSFSb is regarded as ordered instead of randomly distributed for simplification. Optimized $U_{eff} = U-J = 4$ for transition-metal based system (Fe), where J=0 is considered to provide improved accuracy in the calculations. A single oxygen vacancy formation energy was calculated as

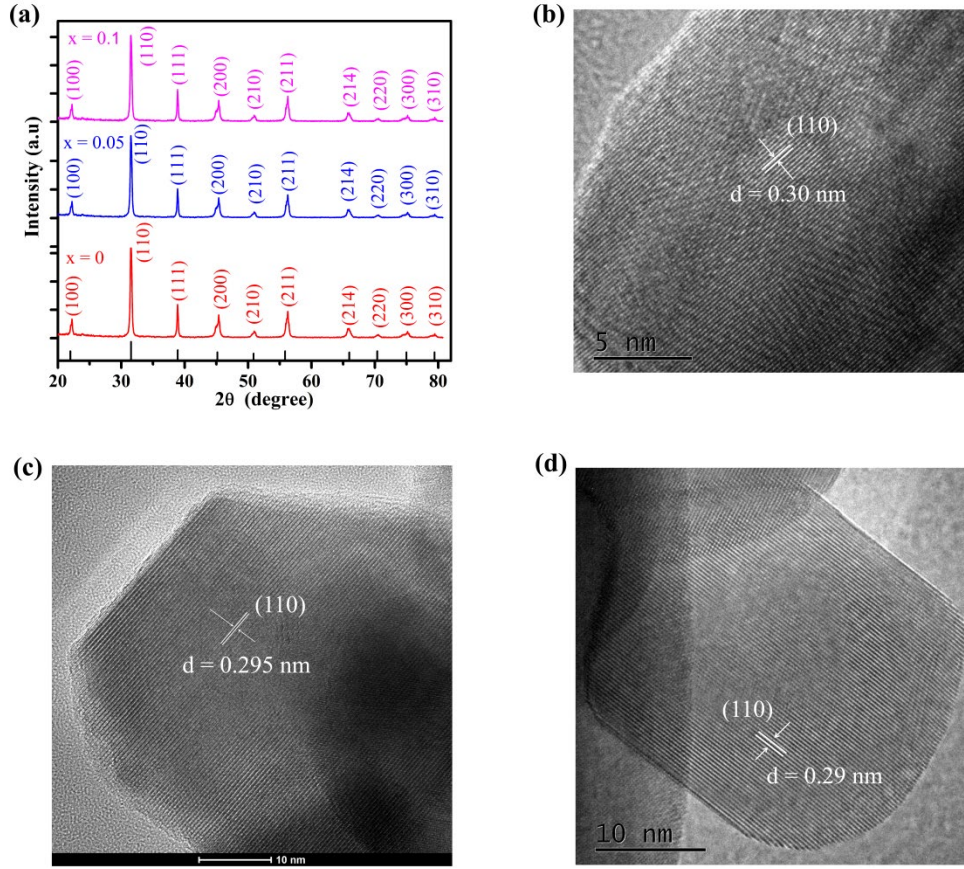$$E_v = E_{tot}(V_O^q) - E_{tot}(ideal) + \mu + q(E_F + E_{valan} + \Delta V)$$

where E_v is the oxygen vacancy formation energy, $E_{tot}(V_O^q)$ is the total energy of the defective superlattice with one oxygen vacancy in charge state q, and q = 0 for a neutral oxygen

vacancy. $E_{tot}(ideal)$ is the total energy of the ideal superlattice, and μ is the oxygen chemical potential. The E_F is referenced to the Fermi level (middle of the valence-band maximum and conduction-band minimum of the perfect superlattice). E_{valan} is the valence-band maximum of the ideal superlattice. The electrostatic potential (ΔV) is in the defective superlattice.

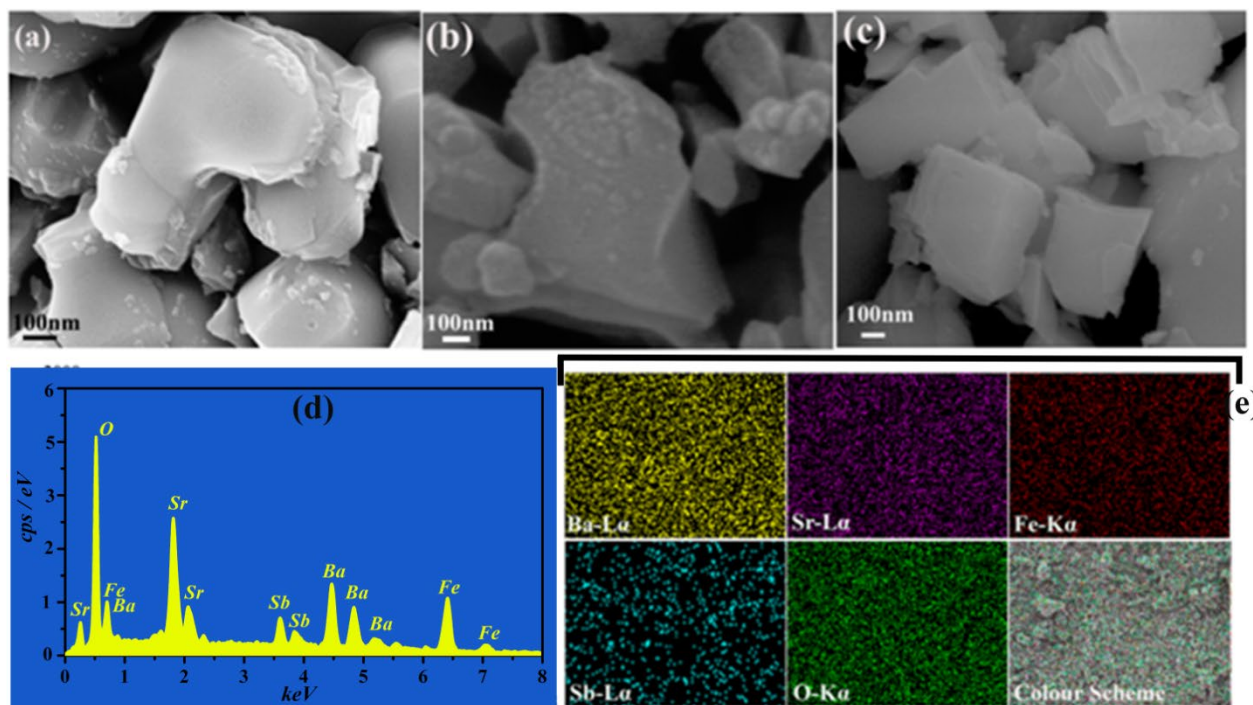## 3 Results and Discussions

3.1 Structural and cation arrangement

Fig. 1a shows XRD diffraction patterns of $Ba_{0.5}Sr_{0.5}Fe_{1-x}Sb_xO_{3-\delta}$ (x = 0, 0.05 and 0.1). The main diffraction peaks are located at 2θ of 23, 32, 39, 46, 57, 68, and 76, which can be indexed to the (021), (110), (111), (200), (211), (220), and (310) planes, respectively, corresponding to the 221 Pm-3m space group (JCPDF # 33-0677) with a lattice constant of 3.940 Å. The lattice constants increase from 3.964 to 3.972 and 3.982 Å for x =0.05 and 0.1, respectively. This increase can be attributed to the difference between the host ionic radii of Fe (0.675 Å) and doped ionic radii of Sb^{5+} (0.76 Å), leading to an expansion of the unit cell. No other peaks with exception of the cubic perovskite phase are observed, indicating Sb ions to be well doped into Fe host lattice [26, 27]. The cubic structure of $Ba_{0.5}Sr_{0.5}FeO_{3-\delta}$ is sustained by doping of Sb ions at the Fe site due to high oxidation state dopant, which may lead to oxygen deficiency in lattice [21, 24]. The d-spacing values are calculated from HRTEM images **Fig. 1(b - d)** using digital micrograph. The d spacing of 0.30 nm, 0.295 nm and 0.29 nm for x=0.1, 0.05 and 0.0 were calculated, respectively. The d-spacing values match 110 lattice planes and well fit to XRD data that unit cell parameters increased with Sb ion doping.

Fig. 1 (a) X-ray diffraction patterns, (b-d) crystal structure of (110) planes obtained by high resolution transmission electron microscopy (HRTEM).

Fig. 2a-c display SEM images of samples, where a large size distribution of the particle for each composition can be seen. However, $Ba_{0.5}Sr_{0.5}Fe_{0.9}Sb_{0.1}O_{3-\delta}$ (x= 0.1) shows homogeneous and fine particles, as compare to observed for x = 0 and 0.05 samples. The average particle sizes are calculated by image J software to be 340 nm, 280 nm and 250 nm for x = 0, 0.05, and 0.1, respectively. In SEM images, particle size is reduced in higher Sb-doping content samples, indicating that Sb-doping inhibits the growth of particles as previously reported [30]. The restrain of agglomerates and the growth of particles in x = 0.1 sample can be attributed to purification by self-diffusion process caused by doping. Dopants literally disperse from the inside to the surface and adjust to restrain particle size and agglomerate formation with concentration of doping, which is a fundamental phenomenon for modification of electronic structures. Therefore, these

can be controlled by manipulating the dopant concentration as reported by Norris et al [31]. The distribution of particles on the surface is also confirmed by EDX particle mapping as shown in **Fig. 2 (d, e)**, and shows a homogenous distribution.

Fig. 2 (a-c) SEM image for powders of $BaSrFe_{1-x}Sb_xO_{3-\delta}$ (x=0, 0.05, 0.1), (d, e) Energy dispersive X-ray analysis (EDX) and particles distribution on surface of $Ba_{0.5}Sr_{0.5}Fe_{0.9}Sb_{0.1}O_{3-\delta}$ respectively.

3.2 Oxygen non-stoichiometry and ORR studies

The results of the TG analysis carried out in air from 30 - 1000°C are shown in **Fig. 3a**. An obvious rapid weight loss around 280°C as also shown by differential thermal analysis curve (DTA). The result implies that the B-site cations in the BSFSb perovskite start to be thermally reduced at around 300 °C. The δ value at room temperature (δ_0), determined by iodometric titration, was 0.18 for the as-synthesized sample and it gradually increases with temperature and reaches a value of 0.32 at 600 °C, which may correspond to the thermally reduction of Fe ions from Fe^{4+} to Fe^{3+} and Fe^{3+} to Fe^{2+} and hence the formation of oxygen vacancies [32]. Moreover, the total
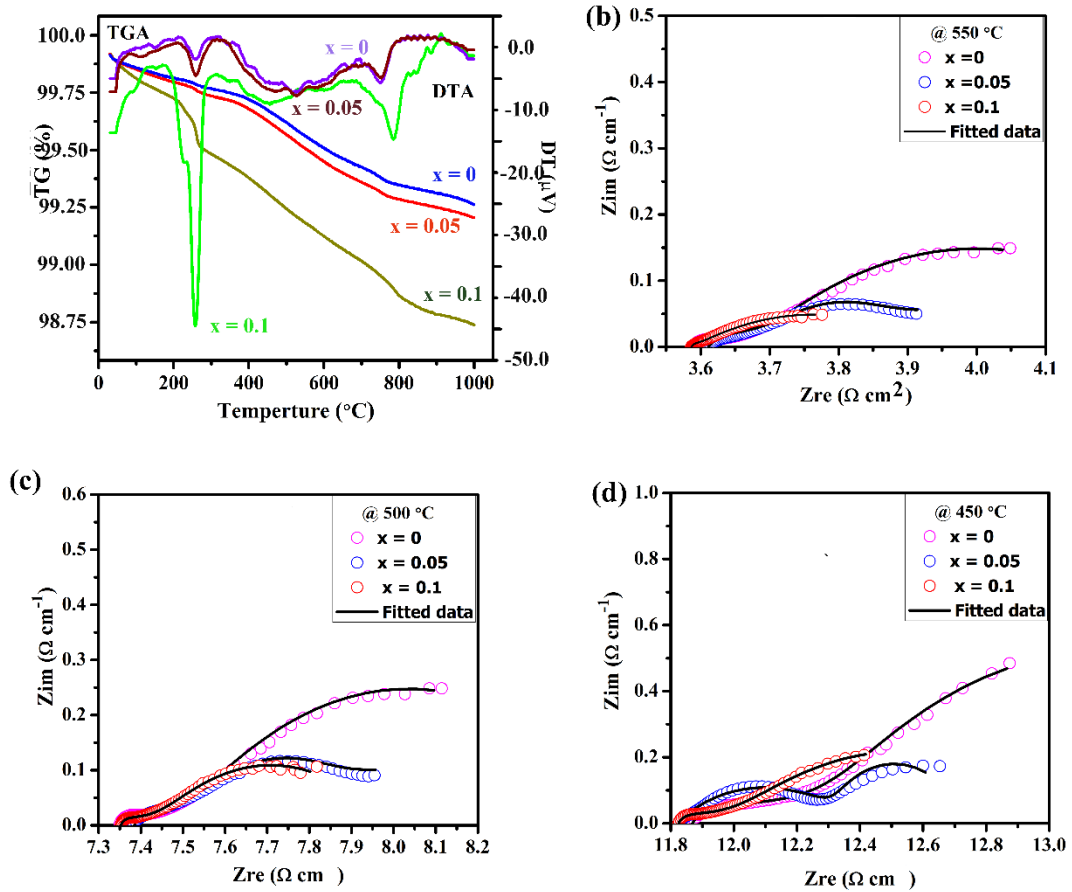
δ value, determined by TGA and iodometric titration method for the as-synthesized sample in air gradually increases with Sb-doping and reaches 0.22, 0.26 and 0.32 for x= 0, 0.05 and 0.1 cathodes, respectively. The weight losses of about 0.30%, 0.38%, and 0.69% for each sample upon heating to 600 ℃ is observed as can be seen in **Fig. 3.3a**. These results show that more oxygen vacancies are generated in Sb-doped samples as compared to un-doped sample and x = 0.1 is with the highest δ value.

To identify ORR characteristics, EIS was examined in a symmetrical cell configuration of BSFSb electrodes and SDC electrolyte at 450, 500 and 550 °C in air. **Fig. 3 (b – d)** presents Nyquist plots of the EIS. However, area-specific resistance (ASR) reflects the overall catalytic activity of cathodes, and low ASR character indicates high ORR characteristic. Measured EIS data are fitted with a model circuit L-R$_o$ (Q$_1$-R$_1$) - (Q$_2$-R$_2$) using Zsimpwin software (as inserted in **Fig. 3 b-d)**. The fitted results describe two dominant polarization processes represented by the ASR at high frequencies (HF) and low frequencies (LF) [33-35]. The ORR is described related to the following steps: i) surface adsorption and dissociation of O$_2$, ii) diffusion of O$_{ad}$, (iii) conversion of O$_{ad}$ into O^{2-} (oxygen ions) and (iv) O^{2-} transport into lattice. Alternatively, a parallel combination of these steps/processes may be involved [36-38].

According to the simulation, the ASR at high frequency is related to charge transfer, and LF is related to the non-charge-transfer process. Since the charge-transfer processes and mass transport interplay with each other to describe total ORR, the fast charge transfer process reflects rapid oxygen diffusion and conversion of molecular oxygen to oxygen ions. As charge transfer involves multi-process steps, e.g., electronic transport to convert to electronic current (e$^-$ charge carriers) with oxygen ion transport to ionic current (O^{2-} charge carriers) and through interface of cathode/electrolyte. Hence, a low ASR of the charge transfer process can be beneficial in many

ways to enhance ORR [34, 36]. Table 1 summarizes the ASR values at high and low frequencies at each temperature. **Fig. 3d** shows that the cell with x = 0.1 exhibits the lowest ASR for both HF and LF processes. Total ASR values of 0.46, 0.77 and 1.53 Ω cm^2 are for x =0, 0.34, 0.65 and 0.83 Ω cm^2 for x = 0.05 and 0.20, 0.50 and 0.62 Ω cm^2 for x = 0.1 at 550, 500 and 450 °C, respectively.

The low ASR of 0.20 Ω-cm^2 in x = 0.1 cell describes the fast charge transfer process due to significantly high oxygen deficiencies produced by Sb doping. The activation energy is also found to be significantly reduced from 49.44 to 32.62 kJ-mol^{-1}, which confirms the high conductivity and ORR activity of x = 0.1 cathode. Therefore, sample (x= 0.1) best fits both theoretical and experimental models to achieve low ASR, which is further described below.

Fig. 3 (a) Thermo-gravimetric analysis (TGA, weight loss) and differential thermal analysis (DTA) of the Ba$_{0.5}$Sr$_{0.5}$Fe$_{1-x}$Sb$_x$O$_{3-\delta}$ (x = 0, 0.05 and 0.1) powders as a function of temperature for calculating oxygen non-stoichiometry at heating

rate of 1°C/min, and (b-d) ORR performance evaluation of prepared $Ba_{0.5}Sr_{0.5}Fe_{1-x}Sb_xO_{3-\delta}$ (x= 0, 0.05 and 0.1) cathode by EIS in a symmetrical cell configuration with SDC ($Sm_{0.2}Ce_{0.8}O_2$) electrolyte in air at 450, 500 and 550 °C.

Table 1. EIS fitted data using ZSIMPWIN software; the R and Q are in units of Ω and $Y_o[S\text{-}sec^\wedge ncm^{-2}]$ where n is Frequency power, n [0<n<1].

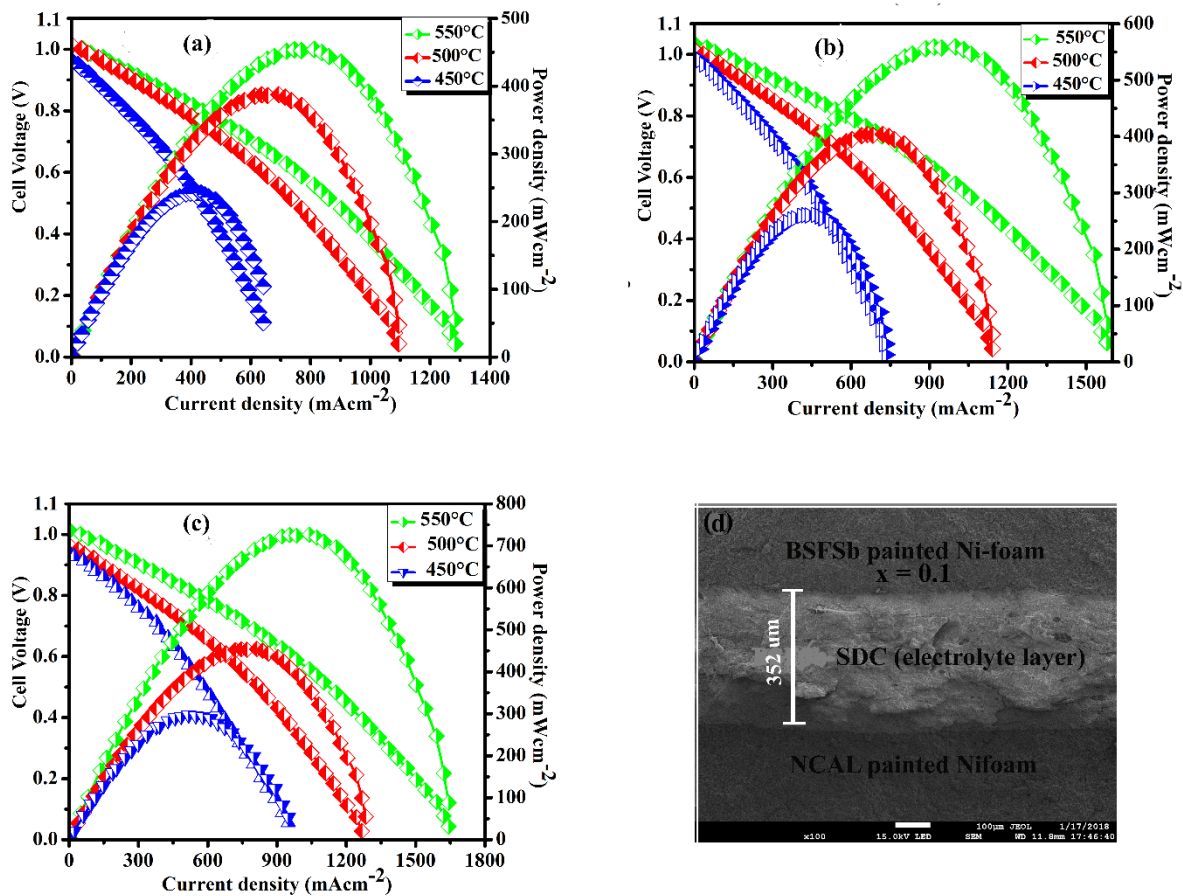| Compositions	Temperature	R_o	R_1	Q_1	n_1	R_2	Q_2	n_2	ASR (total)
x = 0	550 °C	3.58	0.18	0.35	0.25	0.28	0.78	0.65	0.46
	500 °C	7.35	0.29	0.38	0.37	0.48	0.87	0.78	0.77
	450 °C	11.84	0.55	0.40	0.42	0.98	0.95	0.85	1.53
x = 0.05	550 °C	3.57	0.12	0.32	0.22	0.22	0.78	0.58	0.34
	500 °C	7.33	0.18	0.35	0.34	0.48	1.83	0.73	0.65
	450 °C	11.82	0.25	0.37	0.38	0.58	0.92	0.81	0.83
x = 0.1	550 °C	3.56	0.08	0.27	0.18	0.24	0.68	0.45	0.20
	500 °C	7.32	0.14	0.32	0.26	0.36	0.75	0.56	0.50
	450 °C	11.80	0.22	0.34	0.32	0.40	0.80	0.65	0.62

3.3 Fuel cell performance

The ORR catalytic activity of the $Ba_{0.5}Sr_{0.5}Fe_{1-x}Sb_xO_{3-\delta}$ (x= 0, 0.05, and 0.1) is further demonstrated for the cathode in a fuel cell device using the SDC electrolyte. **Fig. 4 (a – c)** shows fuel cell I-V (I-P) characteristics using the cathodes with and without Sb doping. The high values of open circuit voltage (OCV) describe that electrolyte is thick enough without any gas leakage. The peak power densities of 475, 585, and 738 mW cm^{-2} were obtained at 550 °C for x = 0, 0.05 and 0.1 cathode, respectively. The substantial enhancements in power density can be attributed to Sb doping. The x= 0.1 cathode cell also exhibits excellent power density of 460 and 305 mW cm^{-}
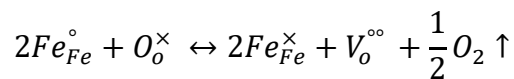
[2] even at low temperatures of 500 and 450°C, respectively. In addition, in order to eliminate the possible contribution from Ni foam, a fuel cell with Ni foam electrode (both cathode and anode) and SDC electrolyte was prepared and tested in the identical procedures and no significant contribution was observed. However, the high-power outputs of the cell indicate the high O^{2-} ion transport and electro-catalytic function in $Ba_{0.5}Sr_{0.5}Fe_{0.9}Sb_{0.1}O_{3-\delta}$. A single performance over a short period of 50 hours using BSFSb (10% Sb doped) cathode is presented in **Fig. S4†,** where device showed a stable behaviour without any significant degradation. Moreover, a cross-section micrograph of the cell with x = 0.1 sample is presented in **Fig. 4d**, where configuration of cell can clearly be seen.

Fig. 4 (a-c) Fuel cell performance evolution of $Ba_{0.5}Sr_{0.5}Fe_{1-x}Sb_xO_{3-\delta}$ (x= 0, 0.05, 0.1) cathodes with-Ni-foam NCAL anode and SDC electrolyte at 450, 500 and 550 °C in H_2/air at the anode and cathode and (d) cross-section SEM image of the cell with x = 0.1 sample respectively.

3.4 Synergistic effects of Sb doping on oxygen vacancy formation and ORR

For further understanding about highly enhanced ORR activity, we performed spectroscopic analysis of the prepare samples. **Fig. 5a** shows the Fe 2p spectra of prepared samples. The Fe 2p peak consists of the two spin–orbit, Fe $2p_{3/2}$ and Fe $2p_{1/2}$ with two doublets satellites. The spin-orbit splitting of Fe 2p electron (Fig. 5a) spectra are well fitted with three valence states, i.e., Fe^{2+}, $Fe^{3+}$and Fe^{4+}, respectively. The peaks at 709.1 and 722.7 eV could be assigned to $Fe^{2+}2p_{3/2}$ and $Fe^{2+}2p_{1/2}$, 710.1 and 724.1 eV are $Fe^{3+}2p_{3/2}$ and $Fe^{3+}2p_{1/2}$, and 712.3 and 725.1 eV to $Fe^{4+}2p_{3/2}$ and $Fe^{4+}2p_{1/2}$, respectively. The percentage of Fe^{2+}, Fe^{3+} and Fe^{4+} is found to be different in each sample, as described by the shifts of Fe-2p toward the low binding energy (BE). According to the peak areas of the singlet curves, the average valence of Fe is found to be 3.08, 2.95 and 2.92 for x = 0, 0.05 and 0.1 at room temperatures, respectively [18]. This observation can be attributed to the partial substitution of Fe with Sb, participation with more mixed oxidation state of Fe (Fe^{4+}/ Fe^{3+} and Fe^{3+}/Fe^{2+}). The chemical shift and valance state of the Fe 2p are indicative of modification in electronic structure with the partial substation of Sb and reduction of Fe valence state could be the result of electronic compensation of donor doping, i.e. Sb doping. Moreover, reduction of Fe cation (Fe^{4+} to Fe^{3+} and Fe^{3+} to Fe^{2+}) with Sb doping results in oxygen vacancy formation. The defect reaction can be written in the Kröger-Vink-notation:

$$2Fe_{Fe}^{\circ} + O_o^{\times} \leftrightarrow 2Fe_{Fe}^{\times} + V_o^{\circ\circ} + \frac{1}{2}O_2 \uparrow$$
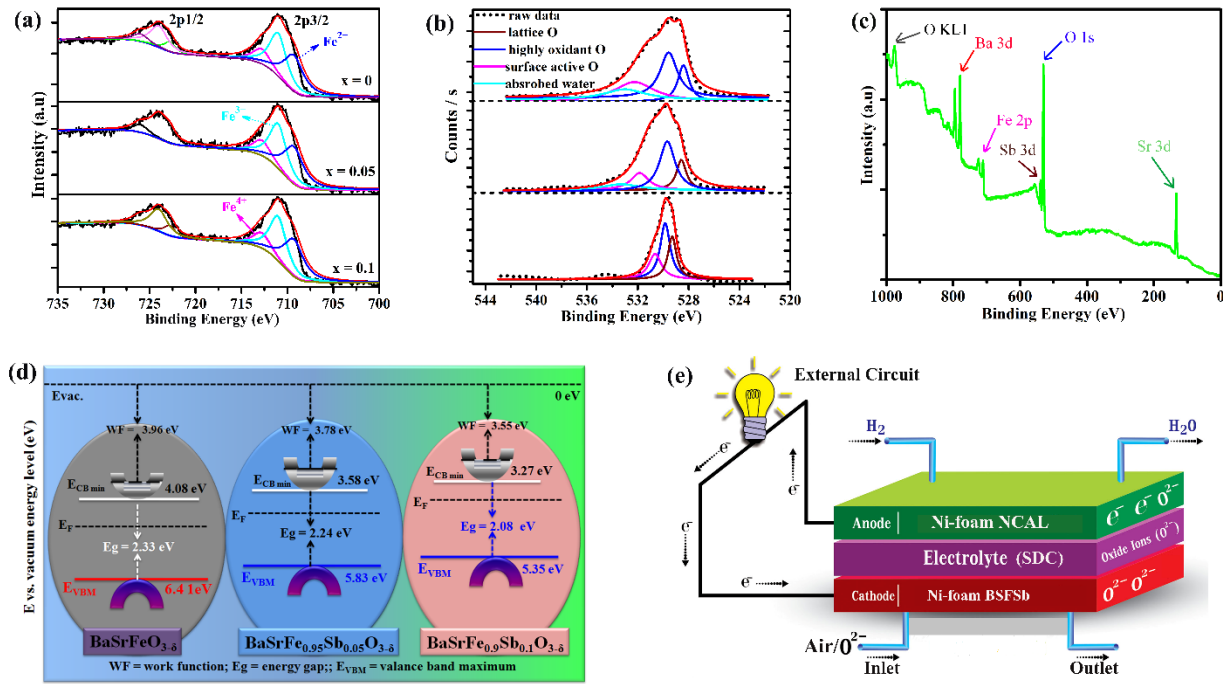
Where Fe_{Fe}° and $Fe_{Fe}^{\times}$ indicate the Fe^{4+} and Fe^{3+} ions, $O_o^{\times}$ and $V_o^{\circ\circ}$ are the lattice oxygen and oxygen vacancy, respectively.

Actually in case of donor doping, the oxygen non-stoichiometry increases with doping due to incorporation of the oxygen on anion site $V_i^{\times}$, where $V_i^{\times}$ and the ionized oxygen vacancy $V_o^{\bullet\bullet}$ cannot be treated as the same species in the defect model due to the different energetic interactions with the oxide anion sub lattice. The high doping contents of Sb^{5+} (10%) added to the $Ba_{0.5}Sr_{0.5}Fe_{1-x}Sb_xO_{3-\delta}$ could results in high concentrations of the interstitial oxygen defects O_i'' occupy the $V_i^{\times}$ sites. Since interstitial oxygen defects in quasi-interstitial sites can be expected to be with much higher concentrations than cation vacancies as reported for other donor doped perovskites oxides [39] **Fig. 5b** shows the O1s spectra of x = 0, 0.05 and 0.1 samples. The O1s spectra of Sb-doped cathode material display two partially superimposed peaks (**Fig. 5a**). There are two major excitations: the first includes O1s of B3d–O2p, Sr 3d-O2p, Fe 2p, and O2p bands and the second, Sb3d-O2p band with binding energy (BE) ranging from 527 to 533 eV. The low BE peak at 527.15-529.4 eV is ascribed to the lattice oxygen (O $_{Lattice}$), and the higher one at 530.3-532.52 eV to the surface-adsorbed oxygen (O surface) species due to surface reconstruction and/or vacancy effects [24]. The high area percentage ratio of O_{ads}/O_{lat} for BSFSb x = 0.1 cathode to x = 0, and 0.05 samples indicates this sample has high oxygen vacancies and good oxygen adsorption capability [21, 28] as described by TG analysis. Another shoulder occurs at 532.5 eV and small shift of O 1s spectra towards higher B.E may be corresponding to highly active surface O in Sb doped samples as compared to un-doped one. The vacancy concentration differences in each sample can also be a main reason for the chemical shift of O1s XPS spectra of Sb-doped cathodes [21].

Moreover, XPS spectra of Ba 3d (5/2, 3/2), Sr 3d (5/2, 3/2) and Sb 3d (5/2, 3/2) are presented in **Fig. S1† (a-c)**. XPS spectra of Sb reveal its higher valance state (Sb^{5+}), acting as a donor doping at room temperature. According to the oxidation state and coordination requirements of the metal ions, Sb^{5+} should coordinated only at tetrahedral site with the oxygen anions,

producing a large concentration of oxygen vacancies on the surface as reported by Min Chen et. al. for LaSrFeCrO$_{3-\delta}$ based perovskite oxide [16]. The Fermi level shifting study is often missing for the oxygen vacancy defect concentration and final state effects contributed to the interpretation problems for many metal oxides [15], which is discussed in next section in details. Further more **Fig. 5c** provides the XPS survey for x = 0.1 samples from 0-1000 eV BE.

Fig. 5 X-ray photoelectron spectroscopy analysis of (a) O1s spectra, (b) Fe 2p spectra of Ba$_{0.5}$Sr$_{0.5}$Fe$_{1-x}$Sb$_x$O$_{3-\delta}$ (x = 0, 0.05 and 0.1) cathodes and (c) XPS survey of x= 0.1 cathode; (d) energy band structure of Ba$_{0.5}$Sr$_{0.5}$Fe$_{1-x}$Sb$_x$O$_{3-\delta}$ (x = 0, 0.05, 0.1) determined by UPS and PL spectra (supporting information **Fig. 2S†**) and (e) schematic diagram for the for the device fabrication and charge transport.

In addition, the effects of Sb doping in the form of oxygen vacancy formation on energy band offsets and Fermi level were determined by, UPS (He 1) and PL (excitation energy ~457 nm) measurements. The results are shown in **Fig. 2S†**. **Fig. 5d** shows a qualitative energy band diagram based on the energy level parameters calculated from UPS and PL spectra for different contents of

Sb-doping. Actually, increase of oxygen vacancies create more electron-rich material (basically more n-type) and shrink the energy gap [40]. Thus, the Fermi level shifts closer to conduction band, and the valance band also moves upward. As a result, the Sb-doped sample's band gap is subsequently reduced. Additionally, a change in E_F and E_{VBM} could enhance DOS near the Fermi level, which increases the efficiency of electron transfer to the adsorbed oxygen species $O_{2,\,ads}$, thus reducing the activation energy and speeding up the ORR process. Fig. 5e presents the schematic diagram for the fuel cell fabrication and charge transport mechamism.

Density functional theory (DFT) calculations can make further understanding for oxide ion diffusion kinetics and mechanisms as reported in literature [41, 42]. For more details about calculation check the above experimental part. The calculations for the oxygen vacancy formation energy by DFT reveal that the Sb-doped structure with x = 0.1 shows much lower oxygen vacancy formation energy (1.325 eV, Fe–$\ddot{V}_o$–Sb) compared with un-doped structures (1.456 eV), which well supports to our above results that the Sb-doped cathode has relatively high oxygen deficiencies with low migration energy. The optimized structures for x = 0, 0.05 and 0.1 cathodes are presented in **Fig. 6a, 6c & 6e**. To study the charge transfer and electron movement the projected density of states (PDOS) for x= 0, 0.05 and 0.1 of each s-orbital, p-orbital and d-orbital are calculated (**Fig. 6b, d & f**). By comparing the PDOS for resolved atomic orbital, the electron density of states (DOS) is very similar except near the Fermi level. For the Sb-doped atoms (**Fig. 6d & 6f**), they exhibit most of DOS of the near the Fermi level and shift of p-band centre more closer to Fermi level (1.52 eV) indicating that Sb-doped is more favourable to increase the DOS of the neighbouring atoms near the Fermi level. Due to the beneficial effect of Sb doping, the DOS of p and d band centre shift near the Fermi level. This enhanced DOS at the Fermi level can increase the efficiency of electron-transfer to the adsorbed oxygen species O_2, ads, and it is

therefore likely that the higher DOS of Fe neighbouring atoms near the Fermi level induced by Sb, is the reason for the faster kinetics of charge-transfer [20] in BSFSb cathode than in un-doped one.

Furthermore, change in energy band gap in the Sb doped sample is also confirmed from DOS, where the Eg values of 2.10 eV, 2.05 eV and 2.01 eV for x = 0, 0.05 and 0.1 cathodes were obtained respectively. The values of Eg from DFT calculation are less than the experimental value, which is common practice that Eg from DFT calculations is always less than the experimental value. Moreover, to visualize the nature of the charge transfer and the chemical bonding, the electronic charge density distribution in 1 0 0 crystallographic planes is calculated as shown in Fig. 6g. Following the Pauling scale, the electro-negativity of Ba, Sr, Fe, Sb and O is in an order of 0.89 < 0.95 0 < 1.78 < 2.05 < 3.44, which indicates that the oxygen atoms exhibit the highest electro negativity. By the removal of a neutral oxygen atom, we find that the oxygen vacancy formation energy decreases, and subsequently delocalization of the extra charge (two excess electrons) left behind by the departing local oxygen redistributed to the ions next to the vacancy. The electron delocalization on oxygen vacancy formation can be the key feature responsible for the very low vacancy formation energy. Nevertheless this, the oxidation state of the cations also does affect the electronic structure for the oxygen vacancy formation [42, 43]; although it is not the controlling factor in such kind of materials.

In fact, we were expecting a similar and even better "local" reduction process in BSFSb, because of the mixed valences states of $Fe^{3+/4+/2+}$. These findings are also in well agreement with our XPS analysis showing that Fe has mixed valance state and Sb^{5+} species dominate at room temperature. As reported, overall decrease energy for vacancy formation is due intrinsic strengths of TM oxo-bonds and intra-atomic exchange energy driving forces. Doubly occupied d-orbital of
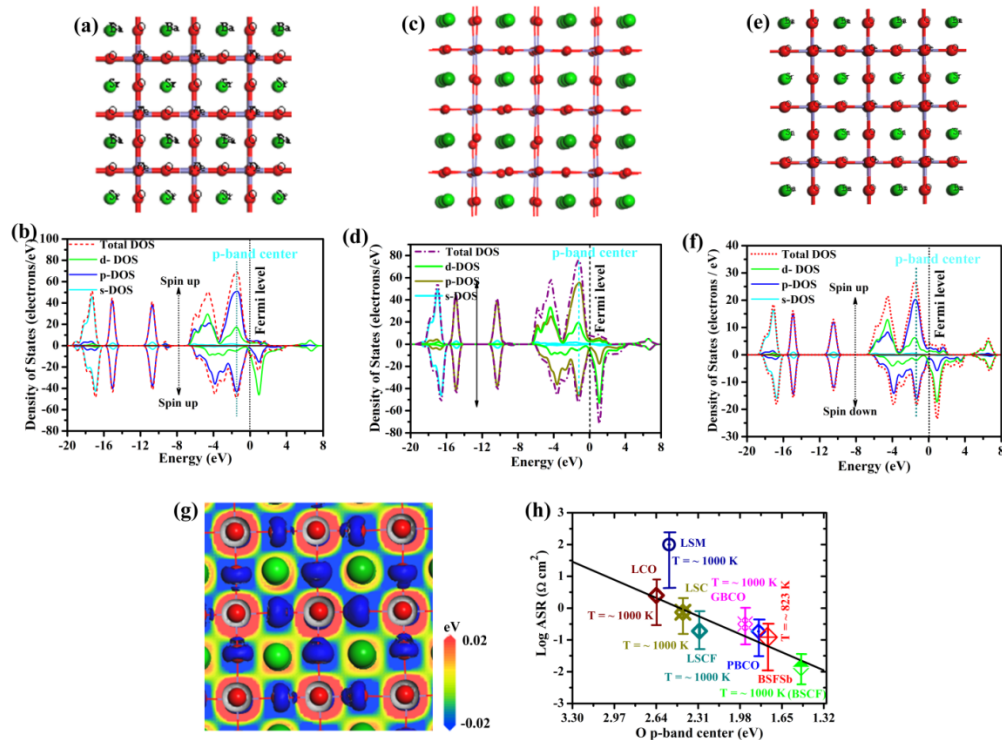
late transition metals (TMs) [44] experience repulsions between metal and oxygen lone pairs and weaken those bonds thus causing efficient charge transfer.

It implies that an efficient charge transfer occurs towards Fe due to excess of two electrons by removal of natural oxygen to form an oxygen vacancy, as also found for low charge transfer resistance in BSFSb by EIS. The electron density for x = 0.1 structure shows atoms surrounded by uniform spheres of charge density and the maximum charge accumulation occurred around Sb and O atoms (Fig. 6g) by the thermo-scale. Moreover, slightly higher electrical conductivity of 8.96 S/cm and low activation energy of 32.62 kJ-mol^{-1} (**Fig. 3S†**) in the x = 0.1 cathode compared to the other two samples make it more feasible for use of ORR electro catalyst. However, the low doping level (up to 10%) of Sb is mainly Sb^{5+} (donor doping), which can increase the overall conductivity [24]. High electronic conductivity found in BSFSb as reported in many doped Fe-rich perovskites, percolation paths have been proposed for electrons movement through the crystal comprised exclusively of Fe$-$O$-$Fe bonds and the excess charge by oxygen vacancy due to dopants. As reported that in Fe rich perovskites [39, 40, 44-46], the $3d_{eg}$ orbital of Fe cations may overlap with the $2p_\sigma$ orbitals of O^{2-} ions to form σ-bonds, and the $3d_{t2g}$ orbital of Fe ions may overlap with the $2p_\pi$ of O^{2-} ions to form π-bonds e.g. e_g–p_σ–e_g and t_{2g}–p_π–t_{2g} bonds. The remarkable improvement of charge transfer in BSFSb cathode can also be likely due to the observed strong hybridization of the Fe and O states at the conduction band edge [45, 46].

To demonstrate the effect of the bulk Op-band centre with ASR, a series of perovskite-type cathode materials reported in the literature is plotted verses their first-principles calculated p-band centre (relative to the Fermi energy) in Fig. 6g. It can be seen from Fig. 6g that log ASRs are almost linearly correlated with the calculated bulk O p-band centre of stoichiometric perovskites, demonstrating that the bulk Op-band centre can be used to describe the ORR activity of the

materials [4]. Since, ASR is a characteristic resistance viewing the overall ORR activity, including both surface and bulk kinetic processes, these two models (ASR and p-band) provide more support to our findings. In lightened of these results, our prepared cathode outperformed most state-of-the-art cathode materials [40-48]. Our both experimental and DFT calculating results reveal that the superior electro catalytic activity of BSFSb that can be the result of a balance of the oxygen vacancy content, oxygen-ion mobility and electron-transfer to O_2, ads, which are imparted by Sb doping. On the other hand, the superior cathodic electro-activity (ORR) can also be attributable to the bulk oxygen ionic conductivity and oxygen surface-exchange kinetics in addition to total conductivity. The higher ionic conductivity can be explained by more oxygen vacancies in $x = 0.1$ relative to other two materials. Thus, these results suggest that sample $x = 0.1$ is the good candidate for fast ionic transport with the synergistic catalytic effects of Sb, which can decrease the energy barrier for oxygen migration (low Ea) and promote transfer of the adsorbed oxygen species $O_{2, ads}$ into O^{2-} for superior ORR activity with reduced ASR as well.

Fig. 6 Optimized structure and their calculated electron partial density of states from calculated using CASTEP density functional theory (a & b) for un-doped $Ba_{0.5}Sr_{0.5}FeO_{3-\delta}$, (c & d) for x =0.05 cathode, and (e & f) (b) for x = 0.1 Sb doped cathodes respectively. (g) electron density difference for x = 0.1 cathode and (h) experimental area specific resistances vs. the calculated bulk Op-band centre of previously reported perovskites cathodes at 1000 K [4, 47, 48] comparisons with our x = 0.1 prepared cathode materials at 823 K. Values with vertical errors bars are the average of multiple data values with an error bar equal to the standard deviation in the mean of the ASR.

4. Conclusion

This work presents an effective approach to design a LT- cathode with enhanced ORR electrocatalytic activity in transition metal oxide-based $Ba_{0.5}Sr_{0.5}Fe_xSb_{1-x}O_{3-\delta}$ perovskite and successfully demonstrate high LTSOFC performances, e.g. 738 mW cm^{-2} at 550°C to provide evidence of the BSFSb-cathode to be an excellent ORR catalyst. We found that an appropriate amount of Sb doping produces more oxygen deficiencies within the $Ba_{0.5}Sr_{0.5}FeO_{3-\delta}$ structure and plays a key role in enhancing ORR activity. The EIS results indicate that the introduction of certain

contents of Sb can significantly improve both the charge and mass transfer processes by promoting bulk diffusion. Both XPS and UPS spectra reveal that Sb doping leads to high oxygen vacancies and make the Fermi level shift closer to the conduction band, and the valance band shift upward as the band gap decreases. Sb doping also increases electron affinity by adding more electrons into the conduction band and provides faster surface electron and ions transfer kinetics. The experimental results are verified by first principle calculations, where Sb-doping significantly makes changes in oxygen p-band center and oxygen vacancy formation energies. Therefore, the obtained results present not only a solution to solve the hurdles of the sluggish kinetics of cathodes for LT-SOFCs but also an effective strategy to design effective electrocatalyst perovskite from a band energy aspect for new advanced LTSOFCs.

Acknowledgement

References

[1] Z. Gao, L. V. Mogni, E. C. Miller, J. G. Railsback, S. A. Barnett, A Perspective on Low-Temperature Solid Oxide Fuel Cells. Energy Environ. Sci. **2016**, 9, 1602.

[2] A. Lashtabeg, S. J. Skinner, Solid Oxide Fuel Cells—a challenge for Materials Chemists?. J. Mater. Chem. **2006**, 16, 3161-3170.

[3] J. Suntivich, H. A. Gasteiger, N. Yabuuchi, H. Nakanishi, J. B. Goodenough, Y. S. Horn, Design Principles for Oxygen-Reduction Activity on Perovskite Oxide Catalysts for Fuel Cells and Metal-Air Batteries. Nat. Chem. **2011**, 3, 546–550.

[4] Y. L. Lee, J. Kleis, J. Rossmeisl, Y. S. Horn, D. Morgan, Prediction of Solid Oxide Fuel Cell Cathode Activity with First-Principles Descriptors. Energy Environ. Sci. **2011**, 4, 3966.

[5] S. Choi, S. Yoo, J. Kim, S. Park, A. Jun, S. Sengodan, Junyoung, Highly Efficient and Robust Cathode Materials for Low-Temperature Solid Oxide Fuel Cells: $PrBa_{0.5}Sr_{0.5}Co_{(2-x)}Fe_{(x)}O_{(5+\delta)}$. Sci. Rep. **2013**, 3, 2426.

[6] Y. Chen, W. Zhou, D. Ding, M. Liu, F. Ciucci, M. Tade, Advances in Cathode Materials for Solid Oxide Fuel Cells: Complex Oxides without Alkaline Earth Metal Elements. Adv. Energy Mater. **2015**, 5, 1500537.

[7] S. B. Adler, Factors Governing Oxygen Reduction in Solid Oxide Fuel Cell Cathodes. Chem. Rev., **2004**, 104, 4791–4843.

[8] A. Chroneos, B. Yildiz, A. Tarancon, D. Parfitt and J. A. Kilner, Oxygen Diffusion in Solid Oxide Fuel Cell Cathode and Electrolyte Materials: Mechanistic Insights from Atomistic Simulations. Energy Environ. Sci. **2011**, 4, 2774–2789.

[9] Y. M. Choi, D. S. Mebane, M. C. Lin, M. L. Liu, Oxygen Reduction on LaMnO3-Based Cathode Materials in Solid Oxide Fuel Cells. Chem. Mater. **2007**, 19, 1690–1699.

[10] A. Evans, J. Martynczuk, D. Stender, C. W. Schneider, T. Lippert, M. Prestat, Low-Temperature Micro-Solid Oxide Fuel Cells with Partially Amorphous $La_{0.6}Sr_{0.4}CoO_{3-\delta}$ Cathodes. Adv. Energy Mater. **2015**, 5, 1400747.

[11] G. Kim, S. Wang, A. J. Jacobson, Oxygen Exchange Kinetics of Epitaxial $PrBaCo_2O_{5+\delta}$ Thin Films. Appl. Phys. Lett. **2006**, 88, 024103.

[12] A. Jun, J. Kim, J. Shin, G. Kim, Perovskite as a Cathode Material: A Review of its Role in Solid-Oxide Fuel Cell Technology. Chem. Electro. Chem. **2016**, 3, 511-530.

[13] C. Xia, M. Liu, Novel Cathodes for Low-Temperature Solid Oxide Fuel Cells. Adv. Mater. **2002**, 14, 521-523.

[14] R. Jacobs, T. Mayeshiba, J. Booske, D. Morgan, Material Discovery and Design Principles for Stable, High Activity Perovskite Cathodes for Solid Oxide Fuel Cells. Adv. Energy Mater. **2018**, 11, 1702708.

[15] F. Dong, Y. Chen, R. Ran, D. Chen, M. O. Tade, S. Liu, Z. Shao, $BaNb_{0.05}Fe_{0.95}O_{3-\delta}$ as a new Oxygen Reduction Electrocatalyst for Intermediate temperature Solid Oxide Fuel Cells. J. Mater. Chem. A, **2013**, 1, 9781-9791.

[16] Min Chen, Scott Paulson, Wang Hay Kan, Venkataraman Thangadurai and Viola Birss, Surface and bulk study of strontium-rich chromium ferrite oxide as a robust solid oxide fuel cell cathode, J. Mater. Chem. A, **2015**, 3, 22614-22626.

[17] J. T. S. Irvine, Perovskite Oxide for Solid Oxide Fuel Cells, Springer, **2009**.

[18] S. Saher, M. Meffert, H. Störmer, D. Gerthsen, H. J. M. Bouwmeester, Grain-size Dependence of the Deterioration of Oxygen Transport for Pure and 3 mol% Zr-Doped $Ba_{0.5}Sr_{0.5}Co_{0.8}Fe_{0.2}O_{3-\delta}$ induced by Thermal Annealing. J. Mater. Chem. A, **2017**, 5, 4982-4990.

[19] C. Duan, D. Hook, Y. Chen, J. Tong, R. O. Hayre, Zr and Y Co-Doped Perovskite as a Stable, High Performance Cathode for Solid Oxide Fuel Cells operating below 500 °C. Energy Environ. Sci. **2017**, 10, 176.

[20] M. Li, M. Zhao, F. Li, W. Zhou, V. K. Peterson, X. Xu1, A Niobium and Tantalum Co-Doped Perovskite Cathode for Solid Oxide Fuel Cells operating below 500 °C. Nat. Commun. **2017**, 8, 13990.

[21] Ainara Aguadero, José Antonio Alonso, Domingo Pérez-Coll, Cristina de la Calle, María Teresa Fernández-Díaz, and John B. Goodenough, $SrCo_{0.95}Sb_{0.05}O_{3-\delta}$ as Cathode Material for High Power Density Solid Oxide Fuel Cells. *Chem. Mater.* 2010, 22, 3, 789–798.

[22] Nak Cheon Jeong, Ji Sun Lee, Eunju Lee Tae, Young Ju Lee, Kyung Byung Yoon, Acidity Scale for Metal Oxides and Sanderson's Electronegativities of Lanthanide Elements. *Angew. Chem. Int. Ed.*, 2008, 47, 10128–10132

[23] Kongfa Chen, Shuai He, Na Li, Yi Cheng, Na Ai, Minle Chen, William D.A.Rickard, Teng Zhang, San Ping Jiang, Nb and Pd co-doped $La_{0.57}Sr_{0.38}Co_{0.19}Fe_{0.665}Nb_{0.095}Pd_{0.05}O_{3-\delta}$ as a stable, high performance electrode for barrier-layer-free Y_2O_3-ZrO_2 electrolyte of solid oxide fuel cells. *J. Power Sources,* 2018, **378**, 433–442.

[24] Lei Gao, Qiang Li, Liping Sun, Tian Xia, Lihua Huo, Hui Zhao and Jean-Claude Grenier, Antimony-doped Bi0.5Sr0.5FeO3-δ as a novel Fe-based oxygen reduction electrocatalyst for solid oxide fuel cells below 600 °C. *J. Mater. Chem. A*, 2018,6, 15221-15229.

[25] Eugene A. Kotomin, Yuri A. Mastrikov, Rotraut Merkle and Joachim Maier., First principles calculations of oxygen reduction reaction at fuel cell cathodes, Curr Opin Electrochem. **2020**, 19, 122-128.

[26] Ana B. Muñoz-García, Andrew M. Ritzmann, Michele Pavone, John A. Keith, and Emily A. Carter, Oxygen Transport in Perovskite-Type Solid Oxide Fuel Cell Materials: Insights from Quantum Mechanics, Acc. Chem. Res. **2014**, 47, 3340-3348.

[27] Hongcan Liu, Wujie Long, Weiwei Song, Jingjun Liu and Feng Wang, Tuning Electronic Band Gap: An Efficient Way to Improve Electrocatalytic Activity of Carbon-Supported Co3O4 Nanocrystals for Oxygen Reduction Reaction. Chem. Eur. J. 2017, 23, 2599-2609.

[28] B. Zhu, B. Wang, Y. Wang, R. Raza, W. Tan, J.S. Kim, Charge Separation and Transport in $La_{0.6}Sr_{0.4}Co_{0.2}Fe_{0.8}O_{3-\delta}$ and Ion-doping Ceria Heterostructure Material for new Generation Fuel Cell. Nano energy, **2017**, 6, 2211-2855.

[29] Naveed Mushtaq, Chen Xia, Wenjing Dong, Baoyuan Wang, Bin Zhu et al., Tuning the Energy Band Structure at Interfaces of the $SrFe_{0.75}Ti_{0.25}O_{3-\delta}$–$Sm_{0.25}Ce_{0.75}O_{2-\delta}$ Heterostructure for Fast Ionic Transport. *ACS Appl. Mater. Interfaces* 2019, 11, 42, 38737–38745.[30] Z. Zhang, Y. Zhu, Y. Zhong, W. Zhou, Z. Shao, Anion Doping: A New Strategy for Developing High-Performance Perovskite-Type Cathode Materials of Solid Oxide Fuel Cells
Adv. Energy Mater. **2017**, 7, 1700242.

[31] Norris DJ, Efros AL, Erwin S. C. Doped Nanocrystals. Science **2008**, 319: 1776–1779.

[32] Lei Gao, Qiang Li, Liping Sun, Xianfa Zhang, Lihua Huo, Hui Zhao, Jean-Claude Grenier, A novel family of Nb-doped Bi0.5Sr0.5FeO3-δperovskite as cathode material for intermediate-temperature solid oxide fuel cells, J. Power Sources. 2014, 258, 76–82.

[33] Naveed Mushtaq, Chen Xia, Wenjing Dong, G. Abbas, Rizwan Raza, Amjad Ali, Perovskite $SrFe_{1-x}Ti_xO_{3-\delta}$ (x < = 0.1) Cathode for low temperature Solid Oxide Fuel Cell. Ceram. Int. **2018**, 44, 10266–10272.

[34] Y. Liu, M. N. Mushtaq, W. Zhang, A. Teng, X. Liu, Single-phase Electronic-Ionic Conducting Sm^{3+}/Pr^{3+}/Nd^{3+} Triple-doped Ceria for new generation Fuel Cell Technology. Int. J. Hydrogen Energy, **2018**, 43 12817-12824.

[35] Li, M. Zhou, W. Peterson, V. K. Zhao, M., Zhu, Z. Systematic Study of Descriptors for Oxygen Evolution Reaction Catalysis in Perovskite Oxides. J. Mater. Chem. A, **2015**, 3, 24064–24070.

[36] A. Aguadero, C. d. l. Calle, J. A. Alonso, M. J. Escudero, M. T. F. Diaz, L. Daza, Structural and Electrical Characterization of the Novel $SrCo_{0.9}Sb_{0.1}O_{3-\delta}$ Perovskite: Evaluation as a Solid Oxide Fuel Cell Cathode Material. Chem. Mater. **2007**, 19, 6437–6444.

[37] D. J. Chen, C. Chen, Z. Zhang, Z. M. Baiyee, F. Ciucci, Z. Shao, Compositional Engineering of Perovskite Oxides for Highly Efficient Oxygen Reduction Reactions. ACS Appl. Mater. Interfaces. **2015**, 7, 8562–8571.

[38] Huang, S. Lu, Q. Feng, S., Li G., Wang, C., $Ba_{0.9}Co_{0.7}Fe_{0.2}Mo_{0.1}O_{3-\delta}$: A Promising Single-Phase Cathode for Low Temperature Solid Oxide Fuel Cells. Adv. Energy Mater. **2011**, 1, 1094–1096.

[39] Yukio Cho, Masayuki Ogawa, Itaru Oikawa, Harry L. Tuller and Hitoshi Takamura, Stabilizing Coexisting n‑Type Electronic and Oxide Ion Conductivities in Donor-Doped Ba−In-Based Oxides under Oxidizing Conditions: Roles of Oxygen Disorder and Electronic Structure, Chem. Mater. **2019**, 31, 2713−2722.

[40] Andrew Bean, Getsoian, Zheng Zhai, and Alexis T. Bell, Band-Gap Energy as a Descriptor of Catalytic Activity for Propene Oxidation over Mixed Metal Oxide Catalysts, J. Am. Chem. Soc. 2014, 136, 13684−13697.

[41] Ana B. Munoz-Garcıa, Michele Pavone, Andrew M. Ritzmann, and Emily A. Carter, Oxide ion transport in $Sr_2Fe_{1.5}Mo_{0.5}O_{6-\delta}$, a mixed ion-electron conductor: new insights from first principles modelling, Phys. Chem. Chem. Phys. **2013**, 15, 6250.

[42] Ana B. Muñoz-García, Daniel E. Bugaris, Michele Pavone, Jason P. Hodges, Ashfia Huq, Fanglin Chen, et al., Unveiling Structure–Property Relationships in $Sr_2Fe_{1.5}Mo_{0.5}O_{6-\delta}$, an Electrode Material for Symmetric Solid Oxide Fuel Cells. J. Am. Chem. Soc. **2012**, 134, 6826−6833.

[43] Zhou W., Ran R., Shao Z., Progress in Understanding and Development of $Ba_{0.5}Sr_{0.5}Co_{0.8}Fe_{0.2}O_{3-\delta}$-based Cathodes for intermediate-temperature Solid-Oxide Fuel Cells: A review. J. Power Sources, **2009**, 192, 231–246.[44] Michele Pavone, Andrew M. Ritzmann, Emily A. Carter, Quantum-Mechanics-based Design Principles for Solid Oxide Fuel Cell Cathode Materials. Energy Environ. Sci., 2011, 4, 4933–4937.[45] Yuri A. Mastrikov, Rotraut Merkle, b Eugene A.

Kotomin, Maija M. Kuklja, Joachim Maier, Surface Termination effects on the Oxygen Reduction Reaction rate at Fuel Cell Cathodes. J. Mater. Chem. A, 2018, 6, 11929–11940.

[46] Y. Zhu, J. Sunarso, W. Zhou, S. Jianga, Z. Shao, High-performance $SrNb_{0.1}Co_{0.9-x}Fe_xO_{3-\delta}$ Perovskite Cathodes for low-temperature Solid Oxide Fuel Cells. J. Mater. Chem. A, **2014**, 2, 15454–15462.

[47] Z. Cai, Y. Kuru, J. W. Han, Y. Chen, B. Yildiz, Surface Electronic Structure Transitions at High Temperature on Perovskite Oxides: The Case of Strained $La_{0.8}Sr_{0.2}CoO_3$ Thin Films. J. Am. Chem. Soc. **2011**, 133, 17696–17704.

[48] Z. P. Shao and S. M. Haile, A High-Performance Cathode for the next generation of Solid-Oxide Fuel Cells. Nature, **2004**, 431, 170–173.